Observation of monopole topological mode

Hengbin Cheng [1,2], Jingyu Yang [1,2], Zhong Wang [3] & Ling Lu [1]✉

Among the many far-reaching consequences of the potential existence of a magnetic monopole, it induces a topological zero mode in the Dirac equation, which was derived by Jackiw and Rebbi 48 years ago and has been elusive ever since. Here, we show that the monopole and multi-monopole solutions can be constructed in the band theory by gapping the three-dimensional Dirac points in hedgehog mass configurations. We then experimentally demonstrate such a monopole bound state in an optimized Dirac acoustic crystal structurally modulated in full solid angles. The monopole mode exhibits the optimal scaling behavior − whose modal spacing is inversely proportional to the cubic root of the modal volume. This work completes the kink-vortex-monopole zero-mode trilogy and paves the way for exploring higher-dimensional bulk-topological-defect correspondence.

The hallmark of topological physics[1–8] is the robust boundary mode protected by the non-trivial bulk gap−known as the bulk-boundary correspondence. As more and more such topological modes have been discovered at various locations in diverse lattice types−such as kinks, edges, surfaces, corners, hinges, vortices, disclinations, and dislocations, there is a growing consensus that a general correspondence exists between the bulk and the topological defects[9–12], where certain order parameters of the lattice change discontinuously. However, among all possible topological defect states up to three dimensions (Fig. 1a), the monopole state remains undiscovered[13].

In topological band theory, the order parameters defining topological defects can be understood as the mass terms[14,15], the scalar or vector parameters that gap out the band degeneracies known as the Dirac points, whose low-energy theory is described by the celebrated Dirac equation. The topological defects of Dirac masses, in one, two, and three dimensions (3D), were first studied by Jackiw, Rebbi, and Rossi[16,17], who derived the zero-energy modes in kink, vortex, and monopole mass settings (Fig. 1b). The kink solution[16], of one mass term, has been realized in polyacetylene as in the Su−Schrieffer−Heeger model[18] in 1D, and on the edge and surface of 2D and 3D topological insulators. The vortex solution[17], of two mass terms, has found connections to the Majorana modes in 2D superconductors[19], the dislocation line states[20,21] in 3D, and has been recently demonstrated in phononic[22–24] and photonic crystals[25–27] based on the Kekulé-distorted graphene model[28].

However, regarding the monopole solution, of full three mass terms in the dimension of our real world where the Dirac equation was originally written, no progress has been made towards its physical discovery since the analytical result was obtained in 1976[16]. In this work, we theoretically propose and experimentally demonstrate this monopole topological mode in a Dirac crystal with hedgehog real-space modulations. We further show that the monopole mode has the optimal mode spacing in the limit of large mode volume.
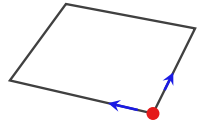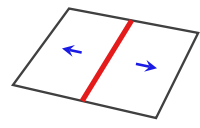
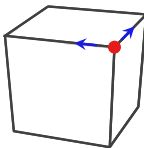## Results

Jackiw−Rebbi monopole mode
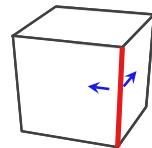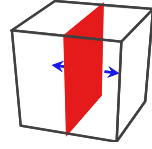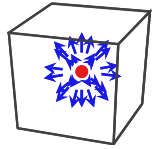
After the proposals of the Dirac monopole in Maxwell's equations[29] and the 't Hooft−Polyakov monopole in Yang−Mills equations[30,31], Jackiw and Rebbi found a zero-mode solution bound to the magnetic monopole in the Dirac equation[16]. The monopole zero mode arises at a 3D topological point defect of three independent mass terms in an 8-by-8 extended Dirac equation shown in Fig. 1b. There has to be a minimal of eight bands to allow three mass terms for the 3D hedgehog construction without breaking the time-reversal symmetry.

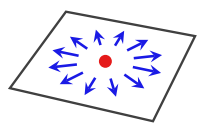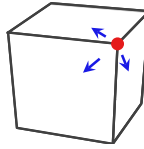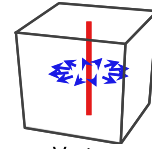We first generalize the Jackiw−Rebbi single-monopole mass profile into the multi-monopole case of arbitrary charges. Although the mass distribution can be chosen to be spherically symmetric for a single monopole, it cannot be for monopoles of charge >1[32]. Our choice of the spatial mapping of the Dirac-mass vectors

[1]Institute of Physics, Chinese Academy of Sciences/Beijing National Laboratory for Condensed Matter Physics, 100190 Beijing, China. [2]School of Physical Sciences, University of Chinese Academy of Sciences, 100049 Beijing, China. [3]Institute for Advanced Study, Tsinghua University, 100084 Beijing, China. ✉e-mail: linglu@iphy.ac.cn

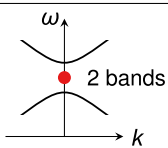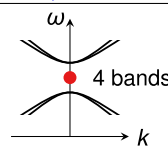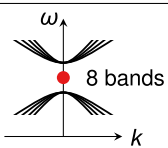**a** Bulk-topological-defect correspondence

b Zero-mode trilogy

Kink (1D)	Vortex (2D)	Monopole (3D)	
Jackiw-Rebbi (1976)	Jackiw-Rossi (1981)	Jackiw-Rebbi (1976)	Theory
$k_x\sigma_3$	$k_x\gamma_{31} + k_y\gamma_{33}$	$k_x\Gamma_{331} + k_y\Gamma_{333} + k_z\Gamma_{310}$	Dirac Hamiltonian
$+m_x\sigma_1 + m'\sigma_2$	$+m_x\gamma_{10} + m_y\gamma_{20} + m'\gamma_{32}$	$+m_x\Gamma_{100} + m_y\Gamma_{200} + m_z\Gamma_{320} + m'\Gamma_{332}$	Mass terms
2 bands	4 bands	8 bands	Band structure
SSH (1979) DFB (1976),VCSEL	HCM (2007) TCSEL (2022)	(This Work)	Lattice model Resonator
FSR $\propto V^{-1}$	FSR $\propto V^{-\frac{1}{2}}$	FSR $\propto V^{-\frac{1}{3}}$	Free spectral range

Fig. 1 | Bulk-topological-defect correspondence and the zero-mode trilogy.
a Summary of the topological modes at topological defects (marked as red points, lines, and plane), where the Dirac mass (with components m_x, m_y, m_z) has an undefined singularity in various dimensions. The blue arrows represent the phase (or sign) of the mass terms in the bulk, on the surface, or on the edge. **b** Zero-mode trilogy. σ_i are the Pauli matrices, $\gamma_{ij} = \sigma_i \otimes \sigma_j$ are the gamma matrices, and $\Gamma_{ijk} = \sigma_i \otimes \sigma_j \otimes \sigma_k$, where $\otimes$ is the Kronecker product. SSH Su–Schrieffer–Heeger[18], HCM Hou–Chamon–Mudry[28], DFB distributed feedback[56], VCSEL vertical-cavity surface-emitting laser[57], TCSEL topological-cavity surface-emitting laser[40]. The scaling behavior between the mode spacing (FSR) and mode volume (V) is listed.

$\hat{\mathbf{m}}(\mathbf{r}) = (\hat{m}_x(\mathbf{r}), \hat{m}_y(\mathbf{r}), \hat{m}_z(\mathbf{r}))$ is expressed as

$$
\begin{aligned}
\hat{m}_x(\mathbf{r}) &= \sin(W_\theta\theta)\cos(W_\phi\phi) \\
\hat{m}_y(\mathbf{r}) &= |\sin(W_\theta\theta)|\sin(W_\phi\phi) \\
\hat{m}_z(\mathbf{r}) &= \cos(W_\theta\theta) \\
W &= \frac{1}{8\pi}\int_A dA\epsilon^{\theta\phi}\epsilon^{xyz}\hat{m}_x\partial_\theta\hat{m}_y\partial_\phi\hat{m}_z = W_\theta W_\phi
\end{aligned}
\tag{1}
$$

where θ and ϕ are the polar and azimuthal angles in the spherical coordinate; W_θ and W_ϕ are the corresponding winding numbers. W is the monopole charge, measuring how many times the three-component Dirac-mass vectors wrap around a closed surface (A)

enclosing the monopole. The absolute value in $\hat{m}_y$ ensured that the 3D wrapping number (W) is expressed by the product of the two angular winding numbers. If we use the standard parametrization without the absolute value[33], $W = \frac{1-(-1)^{W_\theta}}{2}W_\phi$ (see Supplementary Note I for comparison). The reason is that the polar angle $\theta \in [0, \pi]$ generates alternating signs of m_z that unwind each other, while the absolute sign on either m_x or m_y reverses the sign of the in-plane winding wherever m_z unwinds in the polar direction.

In the band-theory language, the above Dirac theory works at the vicinities of the Dirac points in the band structures. The 8-by-8 Dirac equation can be constructed by coupling the two 4-by-4 3D Dirac points. The three mass terms mean three independent ways or perturbations to open the bandgap. In condensed matter, the same low-
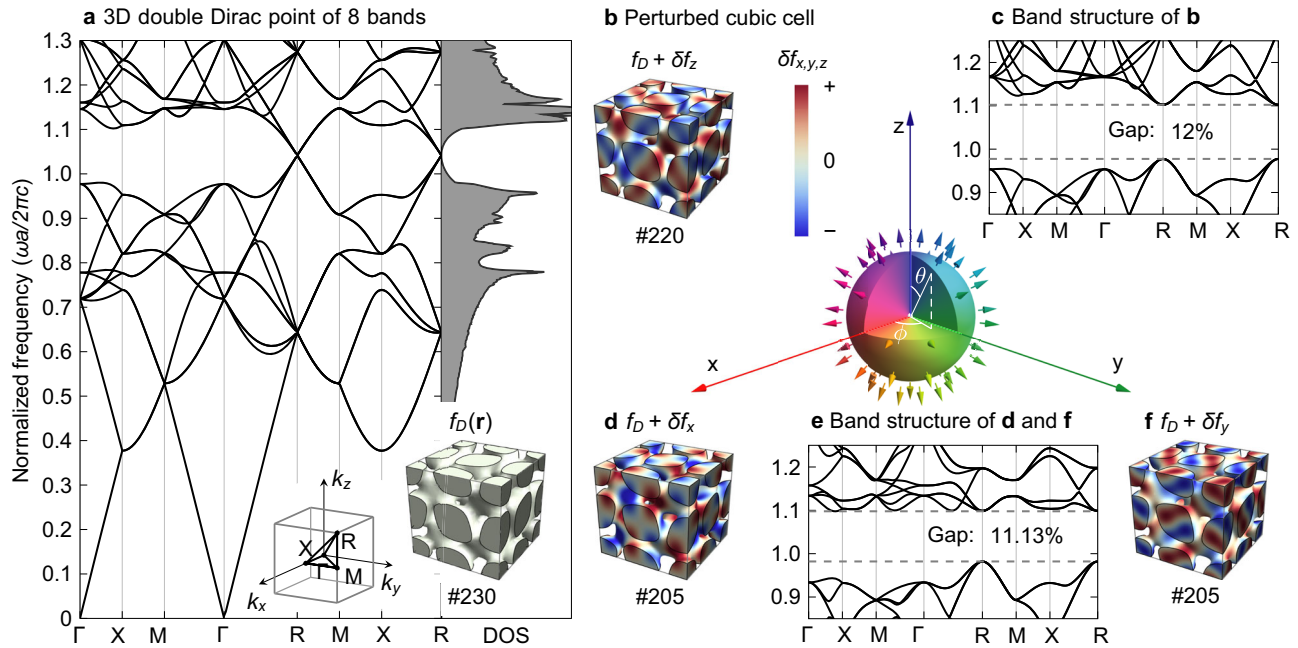
Fig. 2 | Acoustic realization of the double Dirac point and the three mass terms for the monopole design. a The ideal Dirac acoustic crystal with the 8-band Dirac point in the super-cell. **b**, **d**, **f** The perturbed geometries defined by $f_D(\mathbf{r}) + \delta f_i(\mathbf{r})$, $(i = x, y, z)$, whose band structures are plotted in (**c**) and (**e**). The rainbow-colored arrows represent the hedgehog form of the Dirac mass vector (m_x, m_y, m_z).

energy Hamiltonian describes the 3D Majorana zero modes[34,35], although there has been no clue where to find them. In topological-defect classifications[10], the kink, vortex, and monopole zero modes in 1D, 2D, and 3D all belong to the same Altland–Zirnbauer symmetry class BDI with integer invariant ($\mathbb{Z}$) under time-reversal and chiral symmetries. Of course, the chiral symmetry is not rigorously present in our acoustic system, since the spectrum is not exactly up-down symmetric with respect to the Dirac frequency.

Double 3D Dirac point
The starting point of our design is a crystal hosting two 3D Dirac points to form an 8-by-8 Dirac theory. Our Dirac acoustic crystal is defined by the 3D periodic implicit functions

$$f_D(\mathbf{r}) = \sum_{cyc} \sin(\tfrac{4\pi}{a}x) \cos(\tfrac{2\pi}{a}y) \sin(\tfrac{2\pi}{a}z)$$
$$+ 3\sum_{cyc} \cos(\tfrac{4\pi}{a}x) \cos(\tfrac{4\pi}{a}y), \tag{2}$$

where a is the lattice constant and $\sum_{cyc}$ is the sum over the cyclic permutation of (x, y, z). The volume of $f_D(\mathbf{r}) \geq -1.56$ is filled with sound-hard material like plastic, and the rest of the volume is air. This lattice geometry of space group $Ia\bar{3}d$ (#230) is improved upon a previous blue-phase-I (BPI) structure[36–38] to have two fully frequency-isolated Dirac points, locating at the high-symmetry momenta $(\pm P)$ in the Brillouin zone of the body-centered-cubic (BCC) primitive cell (Supplementary Note II). By taking the simple-cubic super-cell as shown in Fig. 2, two Dirac points fold to the momentum R point of the simple-cubic Brillouin zone, forming an 8-by-8 double Dirac point.

Here we explain a general approach to construct photonic and phononic crystals of a specific space group G using triply periodic functions $F_G(\mathbf{r})$, like the one in Eq. (2). This is done through a generic Fourier expansion[39] $F_G(\mathbf{r}) = \sum_i [A_i \cos(\mathbf{k}_i \cdot \mathbf{r}) + B_i \sin(\mathbf{k}_i \cdot \mathbf{r})]$ with the real coefficients A_i and B_i, satisfying $F_G(\mathbf{r}) = F_G(g\mathbf{r})$ for each space-group element $g \in G$. The reciprocal lattice vectors $\mathbf{k} = (l\tfrac{2\pi}{a}, m\tfrac{2\pi}{b}, n\tfrac{2\pi}{c})$ are defined by the lattice constant a, b, c, and integers l, m, n. One usually takes the lowest $l, m,$ and n values for the simplest structures. We use this method to obtain the Dirac structure of Eq. (2) (detailed in

Supplementary Note III), as well as the symmetry-breaking perturbations in Eq. (3) to engineer the Dirac masses.

Dirac-mass engineering
In this section, we present the physical realizations of the mass terms for the double 3D Dirac point through symmetry arguments and space group relations. Each mass term gaps the Dirac degeneracy, by breaking the specific symmetries and reducing the #230 space group to its subgroup. By identifying the corresponding subgroup for each mass term, we can construct the structural perturbations of each subgroup using the periodic-function method described in the previous section.

The total number of four mass terms (m_x, m_y, m_z, m') and their symmetry properties are derived from the low-energy ($\mathbf{k} \cdot \mathbf{p}$) theory of the eight-band Dirac point, given in Fig. 1b and detailed in Supplementary Note IV. All four masses are invariant under time-reversal symmetry, while only m_x is invariant under inversion symmetry (centrosymmetric). The first two masses (m_x, m_y) break the BCC primitive translations and expand the BCC primitive cell to the cubic supercell; they couple the two four-band Dirac points to open a gap and are thus called the "super-cell masses". The latter two masses (m_z, m') break the inversion symmetry to gap the two Dirac points in the BCC primitive cell; they are thus called the "primitive-cell masses".

The two primitive-cell masses (m_z, m') can be realized in the subgroups #220 and #214, respectively. These are the only two BCC subgroups that remain when inversion is removed from #230. They represent two independent ways to break inversion and correspond to the two different masses. Further details on the mass-subgroup relations can be found in Supplementary Note V.

The two super-cell masses (m_x, m_y) can both be realized in the same subgroup #205, the only centrosymmetric subgroup of #230 that remains when the primitive translations are removed. Physically, this implies that the two distinct super-cell masses can be realized by identical structures that are symmetry-related. To understand this, we note that though both masses have inversions in #205, they do not share the same inversion center. This is consistent with the symmetry analysis, which shows that only one super-cell mass, m_x, is invariant
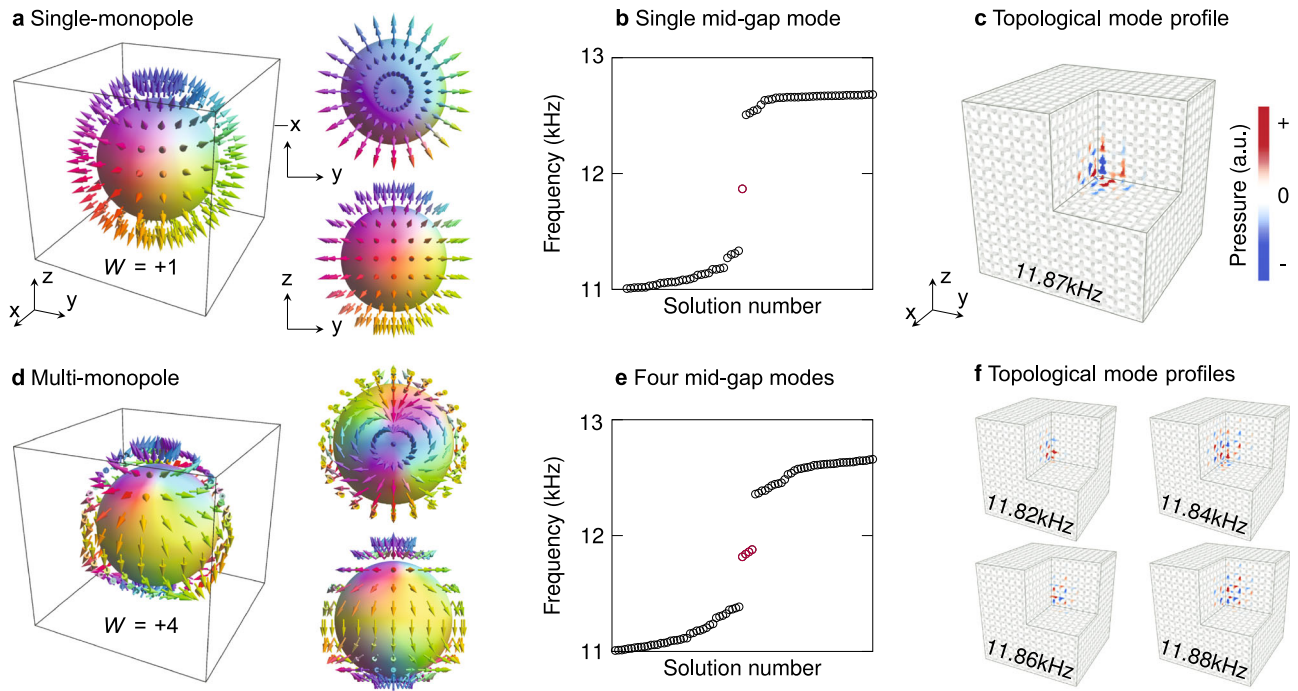
Fig. 3 | Single and multi-monopole cavities. a–c Dirac-mass field, eigenvalue spectrum, and the modal field distribution of the single-monopole cavity. **d–f** Dirac-mass field, eigenvalue spectrum, and the modal field distributions of the multi-monopole cavity with charge four.

under inversion. These two inversion centers, $(0,0,0)$ and $(\frac{1}{4},\frac{1}{4},\frac{1}{4})$, are originally related by the symmetry operations in #230 but absent in #205. One such symmetry is the glide translation $\{M_{01\bar{1}}|(\frac{1}{4},\frac{1}{4},\frac{1}{4})\}$, where $M_{01\bar{1}}$ is a mirror, and squaring the glide is the BCC primitive translation. Correspondingly, m_x and m_y can also be transformed into each other under the glide that translates between the inversion centers. The fact that super-cell masses can be related under fractional lattice translations also appears in the previous low-dimensional examples, such as the SSH model[18], Dirac-vortex cavity[27], and one-way fiber[21].

After identifying the subgroups (#205, #205, #220, #214) for the four Dirac masses (m_x, m_y, m_z, m'), we construct the geometric perturbations (δf_x, δf_y, δf_z, $\delta f'$) within each subgroup. When these perturbations are added to the original #230 structure f_D, they gap the Dirac points. The method for finding these perturbation functions within specific subgroups is identical to that used in finding $f_D(\mathbf{r})$ in Eq. (2).

The functional forms of the first three perturbations are listed in Eq. (3), in which the coefficients (amplitudes) are chosen to maximize the size of the common gap as plotted in Fig. 2. It is easy to check that $\delta f_x(\mathbf{r})$ and $\delta f_y(\mathbf{r})$ are related by the glide symmetry and share the same band structure in Fig. 2e, ensuring the identical bandgap frequencies and size. Since $\delta f'$ (in Supplementary Note VI) opens the smallest bandgap (shown in Supplementary Note VII) compared with the other three masses, we do not include it for the cavity construction.

$$
\begin{aligned}
\delta f_x(\mathbf{r}) &= 0.60 \sum_{\text{cyc}} \cos(\tfrac{4\pi}{a}x)\sin(\tfrac{4\pi}{a}y)\sin(\tfrac{2\pi}{a}z) \\
\delta f_y(\mathbf{r}) &= 0.60 \sum_{\text{cyc}} \sin(\tfrac{4\pi}{a}x)\cos(\tfrac{4\pi}{a}y)\cos(\tfrac{2\pi}{a}z) \\
\delta f_z(\mathbf{r}) &= 0.36 \sum_{\text{cyc}} \cos(\tfrac{4\pi}{a}x)\sin(\tfrac{2\pi}{a}y)\cos(\tfrac{2\pi}{a}z)
\end{aligned}
\tag{3}
$$

Monopole-cavity construction
With three independent mass realizations at hand, we construct the monopole cavity by applying the direction-dependent perturbations to the otherwise uniform 3D Dirac crystal, where (δf_x, δf_y, δf_z) are aligned to the three spatial axes. The geometry of the monopole cavity

is defined by

$$
f_D(\mathbf{r}) + \sum_{i=x,y,z} \hat{m}_i(\mathbf{r},W_\theta,W_\phi)\delta f_i(\mathbf{r}) \geq -1.56
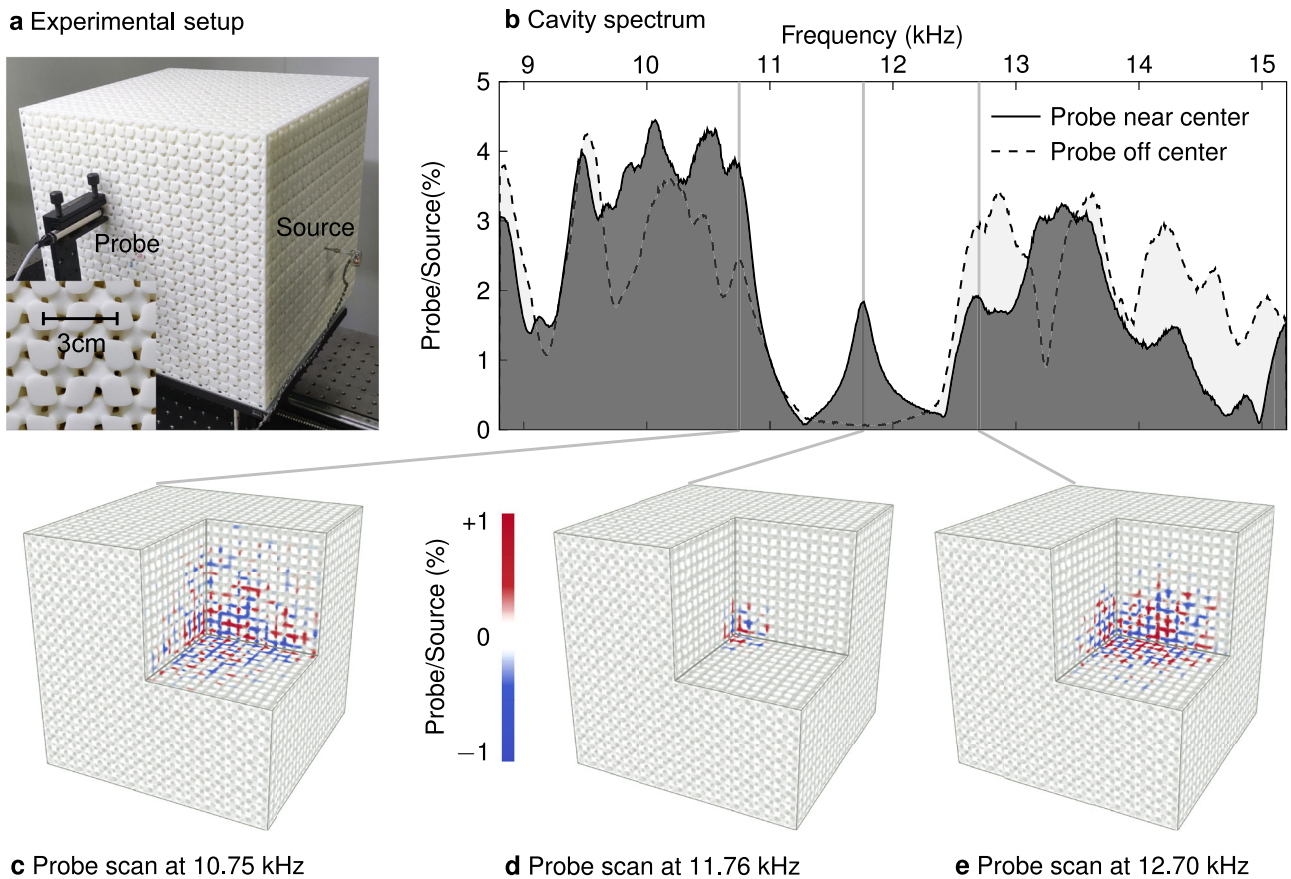\tag{4}
$$

where the hedgehog mass vector $\hat{m}_i(\mathbf{r},W_\theta,W_\phi)$ is given in Eq. (1) with the monopole charge $W = W_\theta W_\phi$.

The numerical results of the single- and multi-monopole modes are presented in Fig. 3. To design the single-monopole cavity, we take $W_\theta = W_\phi = +1$, whose mass field is illustrated in Fig. 3a. A single mid-gap mode appears in the numerical spectrum in Fig. 3b, whose frequency deviation from that of the original Dirac point is less than 1%. Plotted in Fig. 3c is the pressure field of the topological mode localized at the cavity center, with four cubic cells cladding in each direction. To design the multi-monopole cavity, we take $W_\theta = W_\phi = +2$ with $W = +4$ as an example. The high-charge hedgehog field is illustrated in Fig. 3d. The numerical results in Fig. 3e, f show four nearly degenerate mid-gap modes, whose frequency differences are within 1%.

Acoustic experiments
Encouraged by the simulation results, we 3D-print the acoustic monopole cavity with stereolithography using photo-curable resin. As shown in Fig. 4a, the sample has a total volume of $(36\ \text{cm})^3$ and a lattice constant of $a = 3\ \text{cm}$. This bi-continuous structure has two types of through holes, separated by 15 mm $(\tfrac{a}{2})$, whose diameters are about 1.9 and 2.8 mm allowing stainless-steel tubes to get inside the sample for spectral and spatial measurements. The sound source is an earphone whose output tube tip, a diameter of 2.4 mm, is placed near the cavity center. A micro-tube probe (B&K-4182) of diameter 1.2 mm is used to detect the sound pressure at any point in the sample. The acoustic signal is a broadband pulse of a 12.0 kHz central frequency and a 6.4 kHz bandwidth, generated and recorded by a signal analysis module (B&K-3160-A-042), the spectrum recorded in each measurement is averaged a hundred times.

The two spectra in Fig. 4b demonstrate the existence of the bandgap and the localized mid-gap mode. When the probe is off-center, the low signal response indicates a bandgap region roughly

a Experimental setup

b Cavity spectrum

c Probe scan at 10.75 kHz   **d** Probe scan at 11.76 kHz   **e** Probe scan at 12.70 kHz

Fig. 4 | Experimental results on the monopole cavity. a Photograph of the experiment setup and a zoom-in of the sample surface. The 3D-printed cavity has a lattice constant $a = 3$ cm and a sample size of $(12a)^3$. **b** The frequency response of the cavity shows a single mid-gap resonance. **c**–**e** Probe scans of the pressure field distributions inside the sample at three resonant peaks across the bandgap.

from 11 to 12.5 kHz. When the probe is centered, a resonate mode peaks in the middle of the gap at 11.76 kHz, whose quality factor is ~73. The field profiles of the resonant modes are mapped out by scanning the probe tube inside the through holes of the sample using a motorized stage. The pressure fields are recorded, with the step size of 7.5 mm ($= \frac{a}{4}$), on the three orthogonal surfaces crossing the cavity center. In Fig. 4c–e, we plot the signal profiles at the frequencies of the three central resonate modes. It is obvious that only the mid-gap mode is localized as a defect state. The robustness of the topological mode is tested in Supplementary Note VIII, with over a hundred of steel sticks penetrating the cavity.

Optimal scaling behavior

The free spectral range (FSR), of a resonator cavity, is the frequency spacing between adjacent modes that shrinks as the mode volume (V) expands. A wider FSR improves the wavelength-multiplexing bandwidth, the spontaneous emission rate, and the stability of single-mode operation. Although conventional cavities have an inverse proportionality between modal spacing and modal volume (FSR $\propto V^{-1}$), the recent Dirac-vortex cavity[27] exhibits FSR $\propto V^{-\frac{1}{2}}$ that drops much slower than the common scaling rule and is beneficial for broad-area single-mode lasers[40]. Here, we show the monopole cavity offers the optimal scaling of FSR $\propto V^{-\frac{1}{3}}$ (Fig. 1b). A general theoretical argument is given in Supplementary Note IX to derive the above scaling laws using the concept of density-of-states.

We demonstrate numerically, in Fig. 5, the scaling law of the monopole cavity. There are two methods to enlarge the volume of the monopole topological mode. One method is to lower the bandgap size[40], which is twice the FSR for the mid-gap mode. The other method is

to expand the central singular point[27] ($R = 0$) into a volume of non-modulated Dirac lattice with a finite radius R, shown in Fig. 5b inset. As R increases, the volume of the mid-gap mode increases and the high-order cavity modes drop into the bandgap. We take this finite-R method because it requires smaller computational domains and resources. For the same mode volume, the finite-R cavity is more spatially confined than the $R = 0$ version, due to the non-decaying wavefunction in the gapless core and the fastest decaying tails in the cladding region by choosing the largest bandgap. The FSR $\propto V^{-\frac{1}{3}}$ relation is clearly identified in the simulation results from $R = 2a$ to $10a$ in Fig. 5b. Due to the size limitation of 3D-printing and the high acoustic absorption, the experimental verification of the scaling law and the multi-monopole resonances are challenging, as shown in Supplementary Note X. These challenges might be alleviated in photonic platforms.

The unique advantage of the monopole cavity is the robust mechanism in pinning the defect modes at the middle of the bandgap as the FSR is being tuned to zero in a well-controlled fashion. The non-topological defect modes lack the mechanism to stabilize a single mode at the center of the gap in the first place. Comparing with the topological corner modes of third-order 3D topological crystals[41–45], the monopole design avoids sharp interfaces as well as the extra defect modes associated with the additional surfaces and hinges.

Discussion

We experimentally realize the Jackiw–Rebbi monopole mode proposed in their seminar paper from 1976, by observing the topological mode of a 3D topological point defect in a lattice. The method for constructing mass hedgehogs is applicable to other 3D Dirac and Weyl systems[46–50]. Our work completes the zero-mode trilogy, of kink-
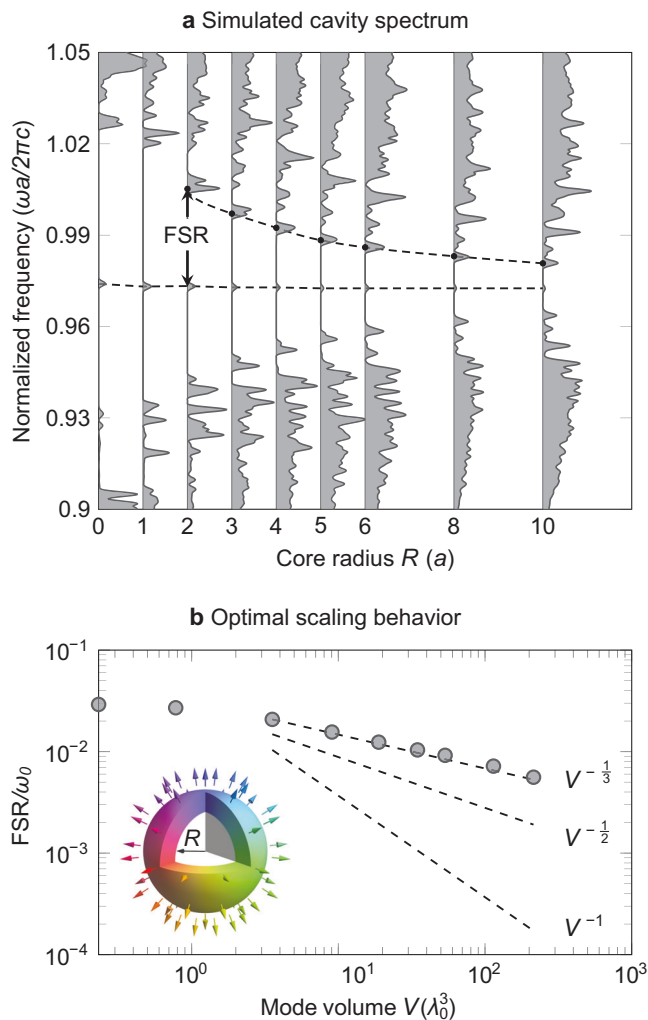
Fig. 5 | Numerical demonstration of FSR $\propto V^{-\frac{1}{3}}$ scaling law of the monopole topological mode at large volumes. a Resonance spectra from the cavities of core radius (R) from 0 to $10a$. The frequency of the monopole topological mode ω_0 remains almost constant in the middle of the bandgaps. **b** Free spectral range versus mode volume (normalized by $\lambda_0 = 2\pi c/\omega_0$) relation fitted with the various scaling powers. The inset illustrates the cavity construction with the monopole core radius R.

vortex-monopole, as well as the bulk-topological-defect correspondence within three spatial dimensions and within Hermitian theory. Extensions to the time dimension (such as instantons[51] and time crystals), synthetic spaces[52,53], as well as non-Hermitian systems can be explored in the future.

Methods

Eigen-frequency solutions
The band structures and eigen-mode solutions are calculated by COMSOL Multiphysics. The solid-air interface is set as hard-wall boundaries. The largest resonator size in computation is $(8a)^3$, taking up the memory size of 380 GB (2666 MHz). The unwanted modes localized at the scattering boundaries can be identified from their low-quality factors.

The mesh generation for large complex structures is challenging. First, we generate the iso-surface mesh from the implicit function using the marching cubes algorithm. Second, we improve the surface meshes with MeshLab[54] using a quadric-based edge collapse strategy. Finally, the improved surface mesh is imported into COMSOL for meshing the bulk with first-order free tetrahedrons. It takes a day to mesh the cavity and another day to compute the eigen-spectrum,

containing 200 eigenmodes around the Dirac frequency, using two Intel Xeon Gold 6140 CPUs of 36 cores at 2.30 GHz.

Time-domain simulations
To further increase the simulation size, for obtaining the scaling law of the monopole resonator, we switch to an open-source time-domain package k-Wave[55]. It is based on pseudo-spectral methods and the geometries are discretized in simple cuboids ($\Delta x = \frac{a}{32}$, $a = 3$ cm). The computation domain includes the cavity volume of $[2(R + 4a)]^3$ with R from 0 to $10a$, one more cell of air surrounding the cavity, and the perfectly matched layers as the boundary condition.

We have to set the solid material parameters very carefully, in order to make the large-scale computation feasible. The two material parameters involved are the mass density (ρ') and the sound velocity (c'), whose product is the sound impedance ($\rho'c'$). First, $\rho'c' \gg \rho_{air}c_{air}$ approximates the hard-wall boundary condition lacked in k-Wave. Second, $c' < c_{air}$ maximizes the time step due to the Courant condition ($\Delta t < \frac{\Delta x}{\sqrt{3}c_{air}} < \frac{\Delta x}{\sqrt{3}c'}$). Third, we set the bulk modulus $\rho'c'^2 \ll \rho_{air}c_{air}^2$ to ensure the numerical stability that we observe in k-wave. The above three conditions lead to our choices of $c' = 10^{-14}$ m/s and $\rho' = 10^{32}$ kg/m³ for the hard material in simulation with $\Delta t = 1.2 \times 10^{-6}$ s.

To obtain the spectral response of the cavity, as in Fig. 5a, we excite the modes with a broadband pulsed source near the cavity center and hundreds of point detectors evenly distributed inside the cavity. After 10^5 time steps, the recorded spectra are averaged and normalized by the source spectrum. To obtain the modal volumes of the monopole topological modes, as in Fig. 5b, we excite the cavity with a narrow-band signal at the resonate frequency and apply a Blackman window with 40,000 time steps. The resulting fields are used to compute the modal volume as $V = \frac{\iiint dxdydz\,|p(\mathbf{r})|^2}{\max[|p(\mathbf{r})|^2]}$, where $p(\mathbf{r})$ is the pressure. The time consumption for the largest cavity of $R = 10a$ is about three weeks, including both the spectral and modal calculations, and the maximum memory in use is about 90 GB.

Data availability
All the relevant data are available from the corresponding author upon request.

References
1. Hasan, M. Z. & Kane, C. L. Colloquium: topological insulators. *Rev. Mod. Phys.* **82**, 3045–3067 (2010).
2. Qi, X.-L. & Zhang, S.-C. Topological insulators and super-conductors. *Rev. Mod. Phys.* **83**, 1057–1110 (2011).
3. Bansil, A., Lin, H. & Das, T. Colloquium: topological band theory. *Rev. Mod. Phys.* **88**, 021004 (2016).
4. Chiu, C.-K., Teo, J. C. Y., Schnyder, A. P. & Ryu, S. Classification of topological quantum matter with symmetries. *Rev. Mod. Phys.* **88**, 035005 (2016).
5. Zhang, X., Xiao, M., Cheng, Y., Lu, M.-H. & Christensen, J. Topological sound. *Commun. Phys.* **1**, 97 (2018).
6. Ozawa, T. et al. Topological photonics. *Rev. Mod. Phys.* **91**, 015006 (2019).
7. Ma, G., Xiao, M. & Chan, C. T. Topological phases in acoustic and mechanical systems. *Nat. Rev. Phys.* **1**, 281–294 (2019).
8. Xue, H., Yang, Y. & Zhang, B. Topological acoustics. *Nat. Rev. Mater.* **7**, 974–990 (2022).
9. Mermin, N. D. The topological theory of defects in ordered media. *Rev. Mod. Phys.* **51**, 591–648 (1979).
10. Teo, J. C. Y. & Kane, C. L. Topological defects and gapless modes in insulators and superconductors. *Phys. Rev. B* **82**, 115120 (2010).
11. Teo, J. C. Y. & Hughes, T. L. Topological defects in symmetry-protected topological phases. *Annu. Rev. Condens. Matter Phys.* **8**, 211–237 (2017).

12. Lin, Z.-K. et al. Topological phenomena at defects in acoustic, photonic and solid-state lattices. *Nat. Rev. Phys.* **5**, 483–495 (2023).

13. Jackiw, R. Fractional and majorana fermions: the physics of zero-energy modes. *Phys. Scr.* **T146**, 014005 (2012).

14. Shen, S.-Q. *Topological Insulators: Dirac Equation in Condensed Matter* (Springer, Singapore, 2017).

15. Schindler, F. Dirac equation perspective on higher-order topological insulators. *J. Appl. Phys.* **128**, 221102 (2020).

16. Jackiw, R. & Rebbi, Cláudio Solitons with fermion number 1/2. *Phys. Rev. D.* **13**, 3398–3409 (1976).

17. Jackiw, R. & Rossi, P. Zero modes of the vortex-fermion system. *Nucl. Phys. B* **190**, 681–691 (1981).

18. Su, W. P., Schrieffer, J. R. & Heeger, A. J. Solitons in polyacetylene. *Phys. Rev. Lett.* **42**, 1698–1701 (1979).

19. Fu, L. & Kane, C. L. Superconducting proximity effect and majorana fermions at the surface of a topological insulator. *Phys. Rev. Lett.* **100**, 096407 (2008).

20. Ran, Y., Zhang, Y. & Vishwanath, A. One-dimensional topologically protected modes in topological insulators with lattice dislocations. *Nat. Phys.* **5**, 298–303 (2009).

21. Lu, L., Gao, H. & Wang, Z. Topological one-way fiber of second chern number. *Nat. Commun.* **9**, 5384 (2018).

22. Gao, P. et al. Majorana-like zero modes in kekulé distorted sonic lattices. *Phys. Rev. Lett.* **123**, 196601 (2019).

23. Chen, C.-W. et al. Mechanical analogue of a majorana bound state. *Adv. Mater.* **31**, 1904386 (2019).

24. Ma, J., Xi, X., Li, Y. & Sun, X. Nanomechanical topological insulators with an auxiliary orbital degree of freedom. *Nat. Nanotechnol.* **16**, 576–583 (2021).

25. Menssen, A. J., Guan, J., Felce, D., Booth, M. J. & Walmsley, I. A. Photonic topological mode bound to a vortex. *Phys. Rev. Lett.* **125**, 117401 (2020).

26. Noh, J. et al. Braiding photonic topological zero modes. *Nat. Phys.* **16**, 989–993 (2020).

27. Gao, X. et al. Dirac-vortex topological cavities. *Nat. Nanotechnol.* **15**, 1012–1018 (2020).

28. Hou, C.-Y., Chamon, C. & Mudry, C. Electron fractionalization in two-dimensional graphenelike structures. *Phys. Rev. Lett.* **98**, 186809 (2007).

29. Dirac, P. A. M. Quantised singularities in the electromagnetic field. *Proc. R. Soc. Lond. Ser. A Contain. Pap. A Math. Phys. Character* **133**, 60–72 (1931).

30. 't Hooft, G. Magnetic monopoles in unified gauge theories. *Nucl. Phys. B* **79**, 276–284 (1974).

31. Polyakov, A. M. Particle spectrum in the quantum field theory. *JETP Lett.* **20**, 194–195 (1974).

32. Weinberg, E. J. & Guth, A. H. Nonexistence of spherically symmetric monopoles with multiple magnetic charge. *Phys. Rev. D.* **14**, 1660–1662 (1976).

33. Shnir, Y. M. *Magnetic Monopoles* Ch. 6 173–239. (Springer, Berlin, Heidelberg, 2005).

34. Teo, J. C. Y. & Kane, C. L. Majorana fermions and non-abelian statistics in three dimensions. *Phys. Rev. Lett.* **104**, 046401 (2010).

35. Nishida, Y., Santos, L. & Chamon, C. Topological superconductors as nonrelativistic limits of Jackiw–Rossi and Jackiw–Rebbi models. *Phys. Rev. B* **82**, 144513 (2010).

36. Cheng, H., Sha, Y., Liu, R., Fang, C. & Lu, L. Discovering topological surface states of Dirac points. *Phys. Rev. Lett.* **124**, 104301 (2020).

37. Lu, L. et al. Symmetry-protected topological photonic crystal in three dimensions. *Nat. Phys.* **12**, 337–U171 (2016).

38. Cai, X. et al. Symmetry-enforced three-dimensional Dirac phononic crystals. *Light: Sci. Appl.* **9**, 38 (2020).

39. Wohlgemuth, M., Yufa, N., Hoffman, J. & Thomas, E. L. Triply periodic bicontinuous cubic microdomain morphologies by symmetries. *Macromolecules* **34**, 6083–6089 (2001).

40. Yang, L., Li, G., Gao, X. & Lu, L. Topological-cavity surface-emitting laser. *Nat. Photonics* **16**, 279–283 (2022).

41. Zhang, X. et al. Dimensional hierarchy of higher-order topology in three-dimensional sonic crystals. *Nat. Commun.* **10**, 1–10 (2019).

42. Xue, H. et al. Realization of an acoustic third-order topological insulator. *Phys. Rev. Lett.* **122**, 244301 (2019).

43. Weiner, M., Ni, X., Li, M., Alù, A. & Khanikaev, A. B. Demonstration of a third-order hierarchy of topological states in a three-dimensional acoustic metamaterial. *Sci. Adv.* **6**, eaay4166 (2020).

44. Liu, S. et al. Octupole corner state in a three-dimensional topological circuit. *Light: Sci. Appl.* **9**, 1–9 (2020).

45. Yang, L. et al. Observation of Dirac hierarchy in three-dimensional acoustic topological insulators. *Phys. Rev. Lett.* **129**, 125502 (2022).

46. Lu, L. et al. Experimental observation of weyl points. *Science* **349**, 622–624 (2015).

47. Armitage, N. P., Mele, E. J. & Vishwanath, A. Weyl and Dirac semimetals in three-dimensional solids. *Rev. Mod. Phys.* **90**, 015001 (2018).

48. Yang, Y. et al. Realization of a three-dimensional photonic topological insulator. *Nature* **565**, 622–626 (2019).

49. Noh, J. et al. Experimental observation of optical Weyl points and fermi arc-like surface states. *Nat. Phys.* **13**, 611–617 (2017).

50. Xia, C.-H., Lai, H.-S., Sun, X.-C., He, C. & Chen, Y.-F. Experimental demonstration of bulk-hinge correspondence in a three-dimensional topological Dirac acoustic crystal. *Phys. Rev. Lett.* **128**, 115701 (2022).

51. Belavin, A. A., Polyakov, A. M., Schwartz, A. S. & Tyupkin, Y. S. Pseudoparticle solutions of the Yang–Mills equations. *Phys. Lett. B* **59**, 85–87 (1975).

52. Yuan, L., Lin, Q., Xiao, M. & Fan, S. Synthetic dimension in photonics. *Optica* **5**, 1396–1405 (2018).

53. Lustig, E. & Segev, M. Topological photonics in synthetic dimensions. *Adv. Opt. Photon.* **13**, 426–461 (2021).

54. Cignoni, P. et al. MeshLab: an open-source mesh processing tool. In *Eurographics Italian Chapter Conference* (eds Scarano, V., Chiara, R. D. & Erra, U.) (The Eurographics Association, 2008).

55. Treeby, B. E. & Cox, B. T. k-wave: Matlab toolbox for the simulation and reconstruction of photoacoustic wave fields. *J. Biomed. Opt.* **15**, 021314 (2010).

56. Haus, H. & Shank, C. Antisymmetric taper of distributed feedback lasers. *IEEE J. Quantum Electron.* **12**, 532–539 (1976).

57. Padullaparthi, B.D., Tatum, J. & Iga, K. *VCSEL Industry: Communication and Sensing* (John Wiley & Sons, 2021).

Acknowledgements

Author contributions

Ling Lu oversaw the project initiated with Zhong Wang. Hengbin Cheng carried out the theoretical analysis, sample designs, and fabrications. Hengbin Cheng performed the numerical simulations and acoustic measurements with the help of Jingyu Yang. Hengbin Cheng and Ling Lu wrote the paper with the inputs from all authors.

Competing interests

The authors declare no competing interests.

Additional information

Publisher's note Springer Nature remains neutral with regard to jurisdictional claims in published maps and institutional affiliations.